Persistent photoconductivity in two-dimensional $Mo_{1-x}W_xSe_2$–$MoSe_2$ van der Waals heterojunctions

Xufan Li,[b] Ming-Wei Lin,[b] and Alexander A. Puretzky
Center for Nanophase Materials Sciences, Oak Ridge National Laboratory, Oak Ridge, TN 37831, USA

Leonardo Basile
Departamento de Física, Escuela Politécnica Nacional, Quito, 17012759, Ecuador

Kai Wang, Juan C. Idrobo, Christopher M. Rouleau, David B. Geohegan, and Kai Xiao[a]
Center for Nanophase Materials Sciences, Oak Ridge National Laboratory, Oak Ridge, TN 37831, USA

(Received 22 September 2015; accepted 4 January 2016)

Van der Waals (vdW) heterojunctions consisting of vertically-stacked individual or multiple layers of two-dimensional layered semiconductors, especially the transition metal dichalcogenides (TMDs), show novel optoelectronic functionalities due to the sensitivity of their electronic and optical properties to strong quantum confinement and interfacial interactions. Here, monolayers of n-type $MoSe_2$ and p-type $Mo_{1-x}W_xSe_2$ are grown by vapor transport methods, then transferred and stamped to form artificial vdW heterostructures with strong interlayer coupling as proven in photoluminescence and low-frequency Raman spectroscopy measurements. Remarkably, the heterojunctions exhibit an unprecedented photoconductivity effect that persists at room temperature for several days. This persistent photoconductivity is shown to be tunable by applying a gate bias that equilibrates the charge distribution. These measurements indicate that such ultrathin vdW heterojunctions can function as rewritable optoelectronic switches or memory elements under time-dependent photo-illumination, an effect which appears promising for new monolayer TMDs-based optoelectronic devices applications.

I. INTRODUCTION

Two-dimensional (2D) layered semiconductors, especially transition metal dichalcogenides (TMDs), have emerged as exciting and versatile materials when their thickness is reduced to a monolayer or few-layers due to the emergence of quantum confinement effects and strong interfacial interactions.[1,2] Stacking different 2D semiconductors into van der Waals (vdW) heterojunctions creates a diverse palette of new, artificially-structured, layered materials with tunable optoelectronic properties depending on the stacking order, relative orientation angle, and atomic registry between the layers. Recently, p–n vdW heterojunctions have been constructed by either stacking or epitaxially growing different layered materials on top of one another or growing them laterally, and have demonstrated desirable optoelectronic functionalities such as photodetectors, photovoltaics, light-emitting diodes, and photodiodes.[3–11] Persistent photoconductivity (PPC), an interesting optoelectronic effect where enhanced electrical conductivity persists after the removal of light illumination,[12–14] has so far received less attention, but has obvious potential for rewritable photoresponsive switches and memory elements.[15]

PPC has been primarily observed in compound semiconductors and layered structures.[16–18] However, 2D materials have suitable properties for PPC that include strong light-matter interaction, high carrier mobility, and gate tunability.[15] While graphene has low photoresponsivity due to its intrinsic metallic property, hybrid graphene structures utilizing quantum dots or MoS_2 atomic layers exhibit interesting PPC properties.[15,19] TMDs, especially MoS_2 and $MoSe_2$, are highly photoresponsive materials with strong optical absorption and band gaps in the visible spectrum. vdW heterostructures constructed from these and other TMDs are good candidates for photoresponsive hybrid materials with charge exchange across the atomically sharp interfaces governed by quantum tunneling transport.

Doping or alloying have proven very effective ways to tune the optical and electrical properties in TMD monolayers.[20,21] Recently, we found that isoelectronic substitution of Mo by W in the monolayer $MoSe_2$ lattice can switch it from n-type to p-type behavior.[22] The resulting alloy, i.e., $Mo_{1-x}W_xSe_2$, has almost the same lattice constant as intrinsic $MoSe_2$, but exhibits a tunable band gap with doping concentration, providing a tunable candidate for the construction of vdW heterojunctions.

Contributing Editor: Joshua Robinson
[a]Address all correspondence to this author.
e-mail: xiaok@ornl.gov
[b]These authors contribute equally to this work.
DOI: 10.1557/jmr.2016.35

In this study, vdW heterojunctions are fabricated by transferring and stacking monolayer single-crystals of $MoSe_2$ and $Mo_{1-x}W_xSe_2$ that were grown by vapor transport methods. The excellent heterojunction quality is assessed by aberration-corrected transmission electron microscopy (TEM), and strong interlayer coupling verified by low-frequency (LF) Raman spectroscopy and photoluminescence (PL). Electrical measurements are used to characterize the p–n junction formed by the stacked $MoSe_2$ and $Mo_{1-x}W_xSe_2$, which are also found to exhibit extremely high photoresponsivity and giant PPC at room temperature. Under time-dependent photoillumination, these heterojunctions can function as rewritable optoelectronic switches or memory elements.

II. EXPERIMENTAL

A. Material growth

Crystalline monolayers of $MoSe_2$ and $Mo_{1-x}W_xSe_2$ were synthesized using a low pressure chemical vapor deposition (CVD) approach that is similar to those described previously.[23] The synthesis was conducted in a tube furnace CVD reactor equipped with a 2 in. quartz tube. In a typical run, the growth substrates, i.e., Si wafer with 250 nm SiO_2 (SiO_2/Si) cleaned by acetone and isopropanol, were placed face down above an alumina crucible containing ~0.2 g of MoO_3 powder (for the growth of $Mo_{1-x}W_xSe_2$, a mixture of MoO_3 and WO_3 powder was used), which was then inserted into the center of the quartz tube. Another crucible containing ~1.2 g Se powder was located at the upstream side of the tube. After evacuating the tube to $\sim 5 \times 10^{-3}$ Torr, flows of 40 sccm (standard cubic centimeter per minute) argon and 4 sccm hydrogen gas were introduced into the tube, and the reaction was conducted at 780 °C (with a temperature ramping rate of 30 °C/min) for 5 min at a reaction chamber pressure of 20 Torr. At 780 °C, the temperature at the location of Se powder was ~290 °C. After growth, the furnace was cooled naturally to room temperature.

B. Monolayer crystal transfer and heterojunction fabrication

For the heterojunction fabrication and TEM sample preparation, poly(methyl methacrylate) (PMMA) was first spun onto the monolayer crystals on the SiO_2/Si substrate at 3500 rpm for 60 s. The PMMA-coated substrate was then floated on 1 M KOH solution that etched silica epilayer, leaving the PMMA film with the monolayer crystals floating on the solution surface. The film was transferred to deionized water several times to remove residual KOH. For TEM samples, the washed film was captured on a Si TEM grid covered by a 50 nm-thick amorphous SiN film with 2 μm windows. For heterojunction fabrication, the film with the monolayer $MoSe_2$ was stacked onto the substrate with the monolayer $Mo_{1-x}W_xSe_2$. The PMMA was removed by acetone and baking at 300 °C in ~30 Torr Ar/H_2 (95%/5%) flowing for 2 h.

C. Device fabrication

Electron beam lithography (FEI DB-FIB with Raith pattern writing software; FEI Company, Hillsboro, Oregon) was used for monolayer $MoSe_2$–$Mo_{1-x}W_xSe_2$ heterojunction device fabrication. A layer of PMMA 495A4 was spun-coat on the SiO_2 (250 nm)/Si substrate with monolayer $MoSe_2$–$Mo_{1-x}W_xSe_2$ heterojunctions, followed by a 180 °C annealing. After pattern writing, development, and lift off, a 10 nm layer of Ti followed by a 50 nm layer of Au was deposited using electron beam evaporation.

D. Characterizations

The morphologies of the monolayer $MoSe_2$ and $Mo_{1-x}W_xSe_2$ crystals were characterized using optical microscopy (Leica DM4500 P, Wetzlar, Germany), scanning electron microscopy (SEM, Zeiss Merlin, Oberkochen, Germany), and atomic force microscopy (AFM, Bruker Dimension Icon, Billerica, Massachusetts). The atomic structures of monolayer $MoSe_2$ and $Mo_{1-x}W_xSe_2$ were investigated via annular dark field (ADF) imaging using an aberration-corrected scanning transmission electron microscope (STEM) (ADF-STEM, Nion UltraSTEM™ 100, Kirkland, Washington) operating at 100 kV, using a half-angle of the ADF detector that ranged from 86 to 200 mrad.

Raman measurements were performed using a micro-Raman system (JobinYvon Horiba, T64000, Edison, New Jersey) based on a triple spectrometer equipped with three 1800 groves/mm gratings and a liquid nitrogen cooled charge-coupled device (CCD) detector. The Raman spectra were acquired under a microscope in backscattering configuration using 532 nm laser excitation (0.1 mW laser power). The excitation laser was focused to a ~1 μm spot using a microscope objective (100x, numeric aperture, N/A = 0.9).

PL measurements were conducted using a home-built micro-PL setup, which included an upright microscope coupled to a spectrometer (Spectra Pro 2300i, Princeton Instruments, Acton, Massachusetts, f = 0.3 m, 150 grooves/mm grating) equipped with a CCD camera (Pixis 256BR, Princeton Instruments). The PL was collected through a 100x objective.

The electrical properties and photoresponse of the monolayer flakes and heterojunctions were measured in vacuum (~10^{-6} Torr) under a probe station using a semiconductor analyzer (Keithley 4200, Keithley Instruments, Cleveland, Ohio) and a laser driven white light source with a power density of 64.42 mW/cm^2 from 400 to 800 nm.

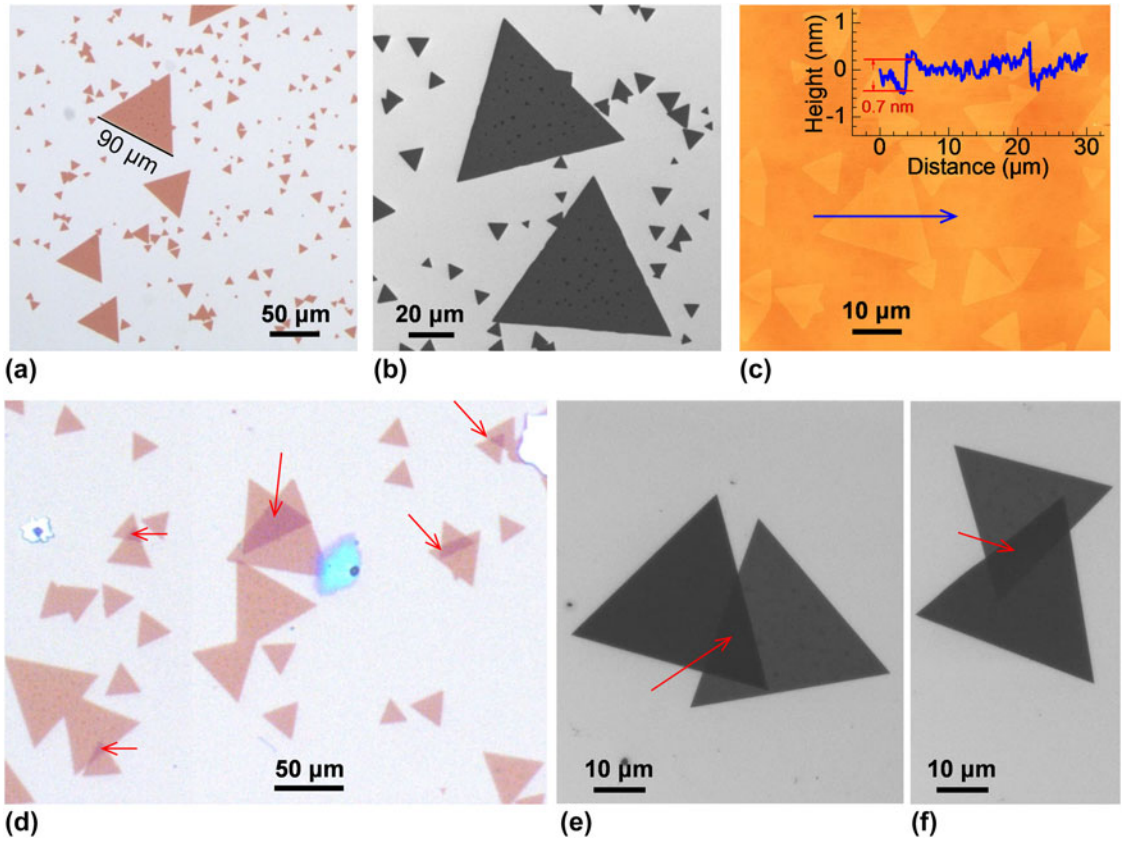

FIG. 1. Morphologies of monolayer $MoSe_2$, $Mo_{1-x}W_xSe_2$, and stacked flakes. (a) Optical micrograph of the monolayer $MoSe_2$ flakes grown on SiO_2/Si substrate. (b) SEM image of the monolayer $Mo_{1-x}W_xSe_2$ flakes grown on SiO_2/Si substrate. (c) AFM image of monolayer $Mo_{1-x}W_xSe_2$ flakes. Inset is the height profile along the solid blue arrow. (d–f) Optical micrograph and SEM images of as-grown monolayer $MoSe_2$ flakes transferred and stacked onto as-grown monolayer $Mo_{1-x}W_xSe_2$ flakes. The solid red arrows indicate the overlapping (junction) region.

III. RESULTS AND DISCUSSION

Figure 1(a) shows an optical micrograph of the as-grown $MoSe_2$ crystalline flakes and Fig. 1(b) shows a SEM image of the as-grown $Mo_{1-x}W_xSe_2$ flakes on SiO_2/Si substrates. The two types of flakes show the same triangular shape and similar sizes ranging from tens to a hundred micrometers. AFM images were used to measure the thickness of these crystals (~0.7nm as in Fig. 1(c)), and correspond to monolayers of $MoSe_2$ and $Mo_{1-x}W_xSe_2$. This indicates that large-sized, uniform monolayer $MoSe_2$ and $Mo_{1-x}W_xSe_2$ were synthesized. To make $MoSe_2$–$Mo_{1-x}W_xSe_2$ heterojunctions, the as-grown monolayer $MoSe_2$ flakes were transferred from the substrate and stacked onto the as-grown monolayer $Mo_{1-x}W_xSe_2$ flakes. The optical micrograph [Fig. 1(d)] and SEM images [Figs. 1(e–f)] show that many stacked flakes are formed with arbitrary interlayer rotation angles, and the overlapping region can be clearly distinguished (as indicated by solid red arrows).

Figure 2(a) shows a typical atomic resolution ADF-STEM (*Z*-contrast) image of an as-grown monolayer of $Mo_{1-x}W_xSe_2$. A hexagonal lattice structure with a lattice constant $a = 0.329$ nm is clearly displayed (see also the fast Fourier transform [FFT] pattern in the inset), which is the same as pristine monolayer $MoSe_2$. The atoms in Fig. 2(a) show different brightness since the intensity of the image is directly related to the atomic number of each atom. Figure 2(b) shows an intensity profile along the solid red arrow in Fig. 2(a), which typically represents the three types of sites in the monolayer $Mo_{1-x}W_xSe_2$. The Se sites show slightly higher intensity than the Mo sites because each Se column contains two atoms, while the sites showing the highest intensity correspond to Mo substituted by W. Therefore, the monolayer $Mo_{1-x}W_xSe_2$ shows alternating atomic arrangement of Mo and Se sites in the hexagonal rings, with the Mo atoms partially and randomly substituted by W atoms. According the ADF-STEM results, the local concentration of W is ~18%. Figure 2(c) shows an ADF-STEM image of a monolayer of $MoSe_2$/$Mo_{1-x}W_xSe_2$ stack. Periodic Moiré patterns are observed due to interlayer rotation, and the FFT pattern [inset of Fig. 2(c)] shows that the two lattices are misaligned by ~15°. The Moiré pattern also indicates that the interface between the two monolayers is clean and atomically sharp.

The optical properties of monolayer $MoSe_2$, $Mo_{1-x}W_xSe_2$, and their stacked heterojunctions [Fig. 3(a)]

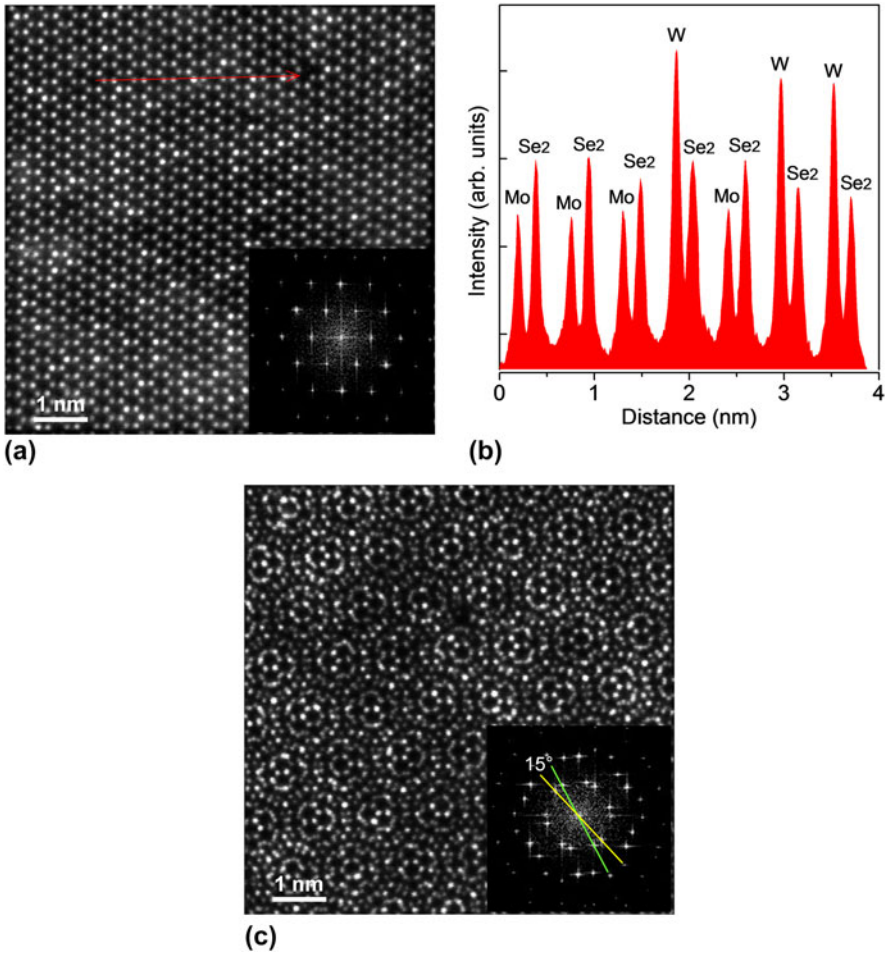

FIG. 2. Atomic structure of monolayer $Mo_{1-x}W_xSe_2$. (a) Atomic-resolution ADF-STEM image of monolayer $Mo_{1-x}W_xSe_2$. Inset is the corresponding FFT pattern. (b) Intensity profiles along the solid red arrow in (a). (c) Atomic-resolution ADF-STEM image of the overlapping (junction) area of two stacked monolayer $MoSe_2$ and $Mo_{1-x}W_xSe_2$. Inset is the corresponding FFT pattern, indicating a 15° of interlayer rotation.

were studied using Raman and PL spectroscopies at room temperature, using 532-nm laser excitation. Three typical Raman modes, i.e., the dominant A_{1g} mode (out-of-plane), and the weak in-plane E_{1g} and E^1_{2g} modes, show up in the Raman spectra of both monolayer $MoSe_2$ and $Mo_{1-x}W_xSe_2$ [Fig. 3(b)].[24] The enlarged Raman spectrum [inset in Fig. 3(b)] indicates that the A_{1g} mode of monolayer $Mo_{1-x}W_xSe_2$ is shifted from 240.9 (monolayer $MoSe_2$) to 242.1 cm^{-1}, which is consistent with previous reported monolayer $Mo_{1-x}W_xSe_2$ alloys.[24] Figure 3(c) shows the room temperature PL spectra of individual monolayers of $MoSe_2$ and $Mo_{1-x}W_xSe_2$. The as-grown monolayer of $MoSe_2$ on SiO_2/Si exhibits a single emission band peaking at ~1.528 eV [Fig. 3(c), solid black curve], corresponding to radiative recombination of the A-exciton in monolayer $MoSe_2$.[25] The A-exciton emission in the as-grown monolayer of $Mo_{1-x}W_xSe_2$ on SiO_2/Si shows a similar band shape, but exhibits a blue-shift of the emission peak to ~1.554 eV [Figs. 3(c) and 3(d), solid red curves] compared with $MoSe_2$. The blue shift can be related to the increase of band gap energy due to W-substitution. Interestingly, compared with the as-grown monolayer $MoSe_2$ and $Mo_{1-x}W_xSe_2$, the transferred monolayers [e.g., the $MoSe_2$ flake shown in Fig. 3(a)] both exhibits blue shift of the emission spectra, peaking at ~1.577 eV [Figs. 3(c) and 3(d), solid green curve, obtained from the spot 1 in Fig. 3(a)] and ~1.603 eV [dashed red curve in Fig. 3(c)], respectively. Such a blue shift can be attributed to the different interaction of the as-grown and transferred monolayers with the substrate.

To study the interlayer coupling in the heterojunction composed of $MoSe_2$ and $Mo_{1-x}W_xSe_2$, monolayers, we measured the PL from the overlapping region of the two flakes shown in Fig. 3(a). The PL intensity from the heterojunction [solid blue curve in Fig. 3(d)] is significantly quenched and the emission band is peaked at a lower energy (i.e., ~1.507 eV) compared with the individual monolayer $MoSe_2$ [solid green curve in Fig. 3(d)] and $Mo_{1-x}W_xSe_2$ [solid red curve in Fig. 3(d)]. The significant PL quenching and red-shifted emission band

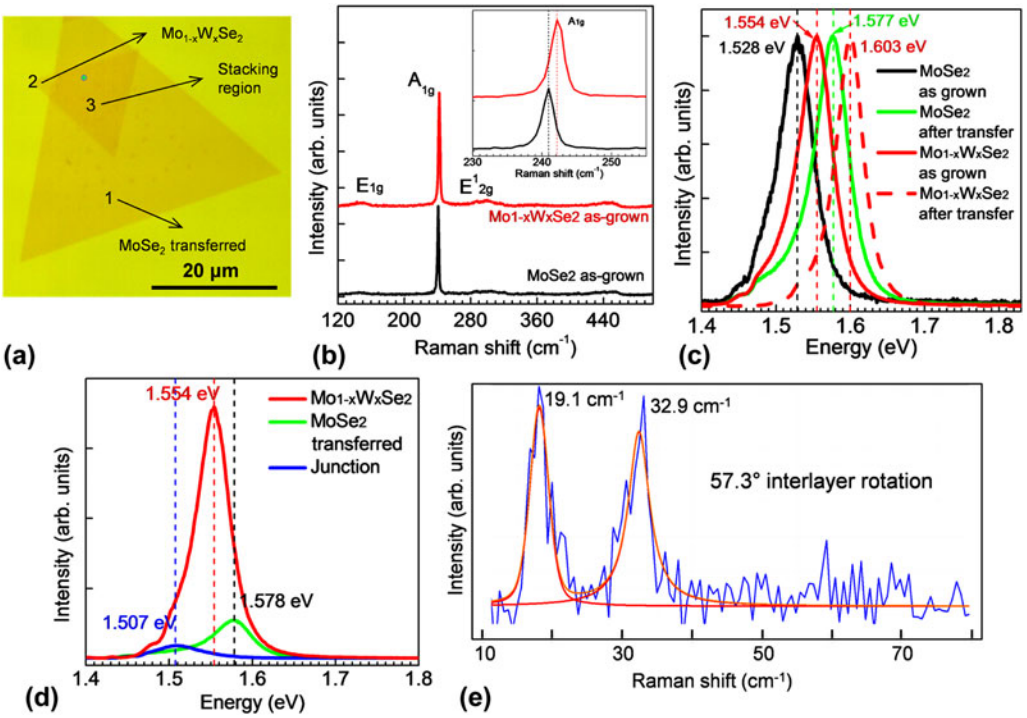

FIG. 3. Optical properties of monolayer $MoSe_2$ and $Mo_{1-x}W_xSe_2$. (a) Optical micrograph of CVD-grown monolayer $MoSe_2$ (larger flake) transferred and stacked onto CVD-grown monolayer $Mo_{1-x}W_xSe_2$ (smaller flake). (b) Raman spectra of the as-grown monolayer $MoSe_2$ (black curve) and $Mo_{1-x}W_xSe_2$ (red curve) with 532 nm laser excitation. Note that the spectra were offset for clarity. (c) Normalized PL spectra of the as-grown monolayer $MoSe_2$ (solid black curve) and $Mo_{1-x}W_xSe_2$ (solid red curve), and the CVD-grown monolayer $MoSe_2$ (green curve) and $Mo_{1-x}W_xSe_2$ (dashed red curve) after transfer with 532 nm laser excitation. (d) PL spectra obtained from spot 1 (transferred CVD-grown monolayer $MoSe_2$), 2 (as-grown monolayer $Mo_{1-x}W_xSe_2$), and 3 (overlapping region) labeled on (a), represented by solid green, red, and blue curves, respectively. (e) LF Raman spectrum (solid blue curve) obtained from the overlapping area in (a). The solid red curve is the calculated LF Raman spectrum.

suggest that the emission from the heterojunction area originates from interlayer charge recombination,[4] and the emergence of such emission also indicates strong interlayer coupling in the stacked heterojunction.

LF (below 50 cm^{-1}) Raman spectroscopy contains rich information regarding the LF shear and breathing modes associated with in-plane and out-of-plane interlayer vibrations of the whole layers, which is an effective and sensitive way to understand the vdW interactions and coupling between layers in stacked 2D crystals.[26] Figure 3(e) shows the LF Raman spectrum obtained from the stacked $MoSe_2/Mo_{1-x}W_xSe_2$ region in Fig. 3(a). Strong, narrow peaks associated with LF shear (at 19.1 cm^{-1}) and breathing (at 32.9 cm^{-1}) modes are observed, which is more evidence for strong interlayer coupling in the heterojunction. According to our previous study on bilayer $MoSe_2$, when the two layers are stacked at exactly 60° interlayer rotation (i.e., 2H stacking configuration), the LF spectrum shows a dominant narrow shear mode peak at 19 cm^{-1} and a very weak, broad feature at ~34 cm^{-1} related to the breathing mode.[26] In the current stacked $MoSe_2/Mo_{1-x}W_xSe_2$ shown in Fig. 3(a), the interlayer rotation is measured to be 57.3°, slightly shifted from perfect 2H stacking, and this leads to significant enhancement of the breathing mode. Such a change in the LF Raman spectrum is attributed to the periodic arrangement of patches with different stacking configurations (i.e., high-symmetry 2H, AB′, A′B stacking and unaligned bilayers) as a result of the slight deviation in the interlayer rotation from 60° (i.e., perfect 2H stacking). Details of this study are presented elsewhere.[27]

To investigate the optoelectronic properties of the $MoSe_2/Mo_{1-x}W_xSe_2$ heterojunction, a device was made by patterning source–drain contacts (Ti/Au) on both flakes while using the highly-doped Si substrate as the back-gating electrode [Fig. 4(a)]. Our previous study has already demonstrated that $MoSe_2$ monolayers showed n-type conduction, which switched to p-type in $Mo_{1-x}W_xSe_2$ monolayers.[22] Indeed, the output (I_{ds}–V_{ds}) curve (at V_{bg} = 0 V) from the $MoSe_2/Mo_{1-x}W_xSe_2$ heterojunction region clearly shows a typical rectifying behavior, with current only being able to pass through the device when the p-type $Mo_{1-x}W_xSe_2$ is forward biased [Fig. 4(b), solid black curve]. To verify that the rectifying behavior originated from the junction, we also measured output curves of the individual $MoSe_2$ and $Mo_{1-x}W_xSe_2$

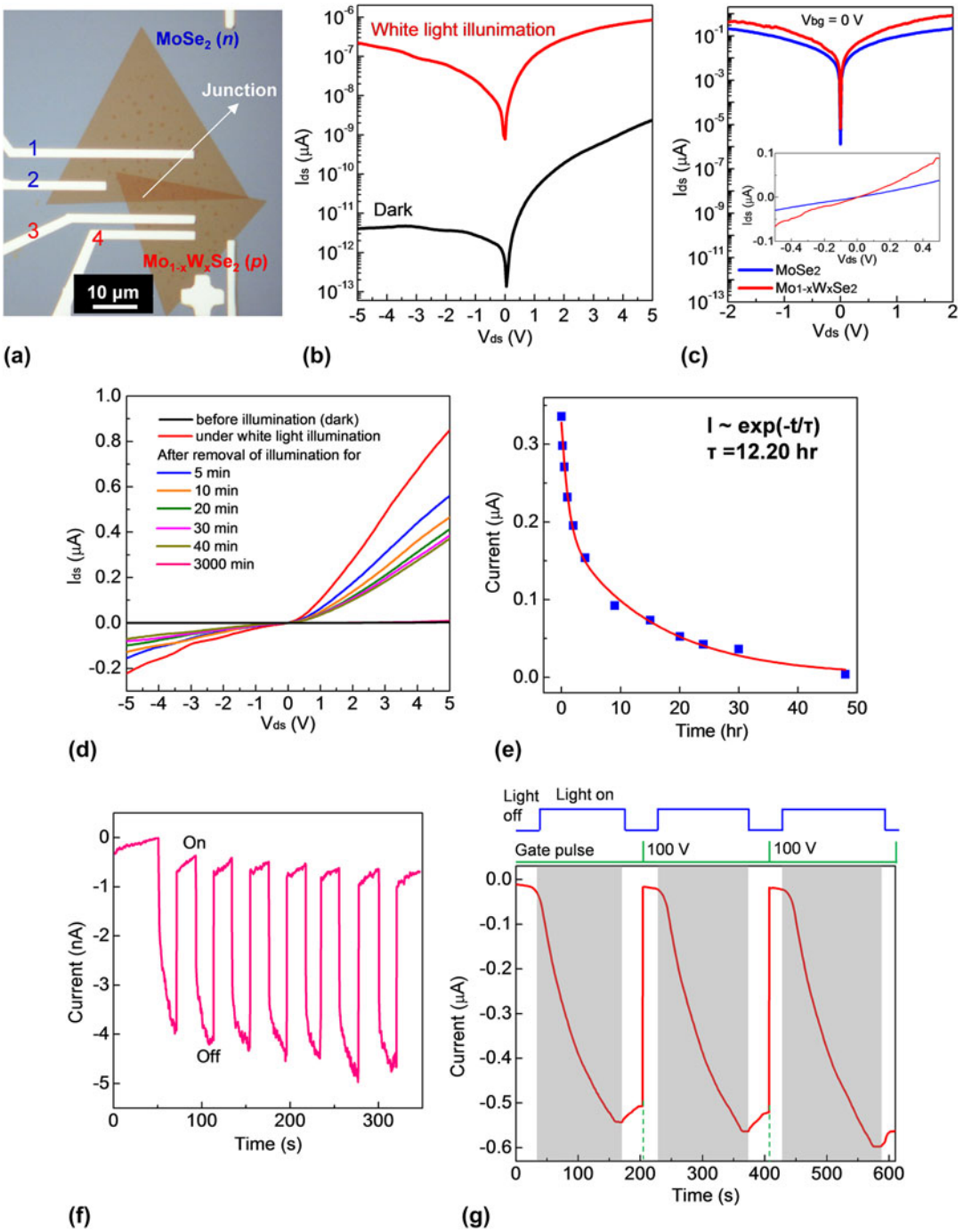

FIG. 4. PPC and photoresponsive switching of the $MoSe_2$–$Mo_{1-x}W_xSe_2$ heterojunction. (a) Optical micrograph of a CVD-grown monolayer $MoSe_2$ (upper flake) transferred and stacked onto a CVD-grown monolayer $Mo_{1-x}W_xSe_2$ (lower flake). The overlapping region of the two flakes forms a heterojunction. Electrodes 1 and 2 were patterned on $MoSe_2$ while 3 and 4 on $Mo_{1-x}W_xSe_2$. (b) I_{ds}–V_{ds} (with I_{ds} shown in absolute values) curves of the heterojunction area shown in (a) on logarithmic scales at zero back-gate voltage in dark (solid black curve) and under white light illumination (solid red curve). (c) I_{ds}–V_{ds} (with I_{ds} shown in absolute values) curves of the individual monolayer $MoSe_2$ (solid blue curve) and $Mo_{1-x}W_xSe_2$ (solid red curve) shown in (a) on logarithmic scales at zero back-gate voltage in dark. Inset is the corresponding I_{ds}–V_{ds} curves on linear scale. (d) I_{ds}–V_{ds} curves of the heterojunction at zero back-gate voltage in dark (solid black curve), under white light illumination (solid red curve), and after removal of the illumination for 5 min (solid blue curve), 10 min (solid orange curve), 20 min (solid green curve), 30 min (solid magenta curve), 40 min (solid yellow curve), and 3000 min (solid pink curve). (e) Decay of the photocurrent after removal of white light source (solid squares), which was fitted exponentially (red curve) with $\tau = 12.2$ h. (f) Time-resolved photoresponse at a bias voltage of -5 V of the individual $Mo_{1-x}W_xSe_2$ flake shown in (a). (g) Photocurrent induction and switching operation of the heterojunction. The gray-shaded areas indicate the presence of white light illumination, during which the current gradually increased to saturation level at $V_{ds} = -5$ V. The green dashed vertical lines indicate the application of gate pulses (100 V), where the current was recovered to the initial level.

flakes in Fig. 4(a). The output curves show linear regions [inset of Fig. 4(c)], indicating Ohmic contacts between the electrodes and flakes. When shown on logarithmic scales, the output curves show very symmetrical behaviors [Fig. 4(c)], demonstrating that the rectifying behavior originated from the p–n heterojunction formed by stacking of $Mo_{1-x}W_xSe_2$ and $MoSe_2$ monolayers. The photoresponse of the heterojunction shown in Fig. 4(a) was studied using a white light lamp with power density of 64.42 mW/cm^2 as the illumination source. Under white light illumination, the I_{ds} (at V_{bg} = 0 V) of the heterojunction was significantly increased by ~3 order of magnitude compared to the dark current, with a photoresponsivity of ~13.2 A/W at V_{ds} = −5 V [Fig. 4(b), solid red curve]. This result demonstrates that the stacked heterojunction have a very good photoresponse. However, after removal of light source, the current in the p–n junction did not immediately decrease back to that originally measured for the dark state; instead, it experienced a fast decay in the first hour and then decreased very slowly, persisting with enhanced photocurrent for more than 2 days [Fig. 4(d)]. The higher conductivity state activated by light exposure persisted for a long time (several days) after the removal of light, showing a giant PPC. The current decay can be fitted exponentially, with a time constant τ of ~12.2 h [Fig. 4(e)]. Interestingly, the PPC was not observed from single monolayers of $MoSe_2$ or $Mo_{1-x}W_xSe_2$, which show fast response time as the light is switched on and off [Fig. 4(f)], typical for the photoresponse behavior of 2D TMDs. It can be concluded that the giant PPC comes only from the junction area. The giant PPC in the monolayer $MoSe_2$–$Mo_{1-x}W_xSe_2$ heterojunction may be due to the following two reasons: (i) the existence of potential barriers or surface barriers on the interface of the heterojunction that spatially separate the photo-generated charge carriers.[18] (ii) The possible existence of traps at the interface of the heterojunction that extend electron-hole recombination lifetime. The detailed mechanism behind the PPC behavior is under further study.

The photoresponse of the $MoSe_2$–$Mo_{1-x}W_xSe_2$ heterojunction was further investigated by studying time-resolved current change at V_{ds} = −5 V. Figure 4(g) shows the result of three photo-illumination cycles. Upon illumination, the photocurrent ($-I_p$) increased gradually and saturated at a certain level after ~120 s (at zero back-gate voltage). After switching the light off, the device showed PPC with slow decay of current (with a time constant τ of ~12.2 h); however, the current could be rapidly and fully recovered to the initial level (dark state) by applying a gate bias pulse at 100 V, which equilibrated the charge distribution. Repeating these steps again resulted in the same behavior, showing the robustness of this heterojunction. Such behavior indicates that the $MoSe_2$–$Mo_{1-x}W_xSe_2$ heterojunction with PPC can potentially be designed to function as photoresponsive memory devices.

In summary, vdW heterostructures were fabricated by transferring and stacking as-grown crystalline monolayers of $MoSe_2$ onto as-grown monolayers of $Mo_{1-x}W_xSe_2$. These heterostructures showed strong interlayer coupling as proven by the emergence of interlayer charge transfer PL and the presence of LF Raman modes. When illuminated with white light, the heterojunction shows extremely high and persistent photocurrent lasting days, which appear applicable for rewritable optoelectronic switch and memory applications involving time-dependent photo-illumination. This $MoSe_2$–$Mo_{1-x}W_xSe_2$ heterojunction can potentially lead to new monolayer TMDs-based optoelectronic devices.

ACKNOWLEDGMENTS

Synthesis science sponsored by the Materials Science and Engineering Division, Office of Basic Energy Sciences, U.S. Department of Energy. Materials characterization conducted at the Center for Nanophase Materials Sciences, which is sponsored at Oak Ridge National Laboratory by the Scientific User Facilities Division, Office of Basic Energy Sciences, U.S. Department of Energy. L.B. acknowledges the financial support of the National Secretariat of Higher Education, Science, Technology and Innovation of Ecuador (SENESCYT). X.L. and M.L. acknowledge support from ORNL Laboratory Directed Research and Development.

REFERENCES

1. S.Z. Bulter, S.M. Hollen, L.Y. Cao, Y. Cui, J.A. Gupta, H.R. Gutiérrez, T.F. Heinz, S.S. Hong, J.X. Huang, A.F. Ismach, E. Johnston-Halperin, M. Kuno, V.V. Plashnitsa, R.D. Robinson, R.S. Ruoff, S. Salahuddin, J. Shan, L. Shi, M.G. Spencer, M. Terrones, W. Windl, and J.E. Goldberger: Progress, challenges, and opportunities in two-dimensional materials beyond graphene. *ACS Nano* **7**, 2898 (2013).
2. B. Radisavljevic, A. Radenovic, J. Brivio, V. Giacometti, and A. Kis: Single-layer MoS_2 transistors. *Nat. Nanotechnol.* **6**, 147 (2011).
3. A.K. Geim and I.V. Grigorieva: van der Waals heterostructures. *Nature* **499**, 419 (2013).
4. H. Fang, C. Battaglia, C. Carraro, S. Nemsak, B. Ozdol, J.S. Kang, H.A. Bechtel, S.B. Desai, F. Kronast, A.A. Unal, G. Conti, C. Conlon, G.K. Palsson, M.C. Martin, A.M. Minor, C.S. Fadley, E. Yablonovitch, R. Maboudian, and A. Javey: Strong interlayer coupling in van der Waals heterostructures built from single-layer chalcogenides. *Proc. Natl. Acad. Sci. U. S. A.* **111**, 6198 (2014).
5. C-H. Lee, G-H. Lee, A.M. van der Zande, W. Chen, Y. Li, M. Han, X. Cui, G. Arefe, C. Nuckolls, T.F. Heinz, J. Guo, J. Hone, and P. Kim: Atomically thin p-n junctions with van der Waals heterointerfaces. *Nat. Nanotechnol.* **9**, 676 (2014).
6. R. Cheng, D. Li, H. Zhou, C. Wang, A. Yin, S. Jiang, Y. Liu, Y. Chen, Y. Huang, and X. Duan: Electroluminescence and photocurrent generation from atomically sharp WSe_2/MoS_2 heterojunction p-n diodes. *Nano Lett.* **14**, 5590 (2014).

7. M-H. Chiu, C. Zhang, H-W. Shiu, C-P. Chuu, C-H. Chen, C-Y.S. Chang, C-H. Chen, M-Y. Chou, C-K. Shih, and L-J. Li: Determination of band alignment in the single-layer MoS_2/WSe_2 heterojunction. *Nat. Commun.* **6**, 7666 (2015).
8. P. Rivera, J.R. Schaibley, A.M. Jones, J.S. Ross, S. Wu, G. Aivazian, P. Klement, K. Seyler, G. Clark, N.J. Ghimire, J. Yan, D.G. Mandrus, W. Yao, and X. Xu: Observation of long-lived interlayer excitons in monolayer $MoSe_2$-WSe_2 heterostructures. *Nat. Commun.* **6**, 6242 (2015).
9. X. Hong, J. Kim, S-F. Shi, Y. Zhang, C. Jin, Y. Sun, S. Tongay, J. Wu, Y. Zhang, and F. Wang: Ultrafast charge transfer in atomically thin MoS_2/WS_2 heterostructures. *Nat. Nanotechnol.* **9**, 682 (2014).
10. S. Tongay, W. Fan, J. Kang, J. Park, U. Koldemir, J. Suh, D.S. Narang, K. Liu, J. Ji, J. Li, R. Sinclair, and J. Wu: Tuning interlayer coupling in large-area heterostructures with CVD grown MoS_2 and WS_2 monolayers. *Nano Lett.* **14**, 3185 (2014).
11. F. Withers, O. Del Pozo-Zamudio, A. Mishchenko, A.P. Rooney, A. Gholinia, K. Watanabe, T. Taniguchi, S.J. Haigh, A.K. Geim, A.I. Tartakovskii, and K.S. Novoselov: Light-emitting diodes by band-structure engineering in van der Waals heterostructures. *Nat. Mater.* **14**, 301 (2015).
12. K. Shimakawa: Persistent photocurrent in amorphous chalcogenides. *Phys. Rev. B* **34**, 8703 (1986).
13. K. Okamoto, H. Sato, K. Saruwatari, K. Tamura, J. Kameda, T. Kogure, Y. Umemura, and A. Yamagishi: Persistent phenomena in photocurrent of niobate nanosheet. *J. Phys. Chem. C* **111**, 12827 (2007).
14. P. Feng, I. Mönch, S. Harazim, G. Huang, Y. Mei, and O.G. Schmidt: Giant persistent photoconductivity in rough silicon nanomembranes. *Nano Lett.* **9**, 3453 (2009).
15. K. Roy, M. Padmanabhan, S. Goswami, T.P. Sai, G. Ramalingam, S. Raghavan, and A. Ghosh: Graphene-MoS_2 hybrid structures of multifunctional photoresponsive memory devices. *Nat. Nanotechnol.* **8**, 826 (2013).
16. X.Z. Dang, C.D. Wang, E.T. Yu, K.S. Boutros, and J.M. Redwing: Persistent photoconductivity and defect levels in n-type AlGaN/GaN heterostructures. *Appl. Phys. Lett.* **72**, 2745 (1998).
17. A. Horn, O. Katz, G. Bahir, and J. Salzman: Surface states and persistent photocurrent in a GaN heterostructure. *Semicond. Sci. Technol.* **21**, 933 (2006).
18. A. Tebano, E. Fabbri, D. Pergolesi, G. Balestrino, and E. Traversa: Room-temperature giant persistent photoconductivity in $SrTiO_3$/$LaAlO_3$ heterostructures. *ACS Nano* **6**, 1278 (2012).
19. G. Konstantatos, M. Badioli, L. Gaudreau, J. Osmond, M. Bernechea, F.P. Garcia de Arquer, F. Gatti, and F.H.L. Koppens: Hybrid graphene-quantum dot phototransistors with ultrahigh gain. *Nat. Nanotechnol.* **7**, 363 (2012).
20. Y. Gong, Z. Liu, A.R. Lupini, G. Shi, J. Lin, S. Najmaei, Z. Lin, A.L. Elias, A. Berkdemir, G. You, H. Terrones, M. Terrones, R. Vajtai, S.T. Pantelides, S.J. Pennycook, J. Lou, W. Zhou, and P.M. Ajayan: Band gap engineering and layer-by-layer mapping of selenium-doped molybdenum disulfide. *Nano Lett.* **14**, 442 (2014).
21. J. Suh, T-E. Park, D-Y. Lin, D. Fu, J. Park, H.J. Jung, Y. Chen, C. Ko, C. Jang, Y. Sun, R. Sinclair, J. Chang, S. Tongay, and J. Wu: Doping against the native propensity of MoS_2: Degenerate hole doping by cation substitution. *Nano Lett.* **14**, 6976 (2014).
22. X. Li, M-W. Lin, B. Huang, L. Basile, S.M. Hus, A.A. Puretzky, C-H. Chen, J. Lee, K. Wang, J.C. Idrobo, M. Yoon, A.P. Li, C.M. Rouleau, B.G. Sumpter, D.B. Geohegan, and K. Xiao: Isoelectronic tungsten doping in monolayer $MoSe_2$: From carrier type modulation to p–n homojunction. Unpublished.
23. H. Li, X. Duan, X. Wu, X. Zhuang, H. Zhou, Q. Zhang, X. Zhu, W. Hu, P. Ren, P. Gao, L. Ma, X. Fan, X. Wang, J. Xu, A. Pan, and X. Duan: Growth of alloy $MoS_{2x}Se_{2(1-x)}$ nanosheet with fully tunable chemical compositions and optical properties. *J. Am. Chem. Soc.* **136**, 3756 (2014).
24. M. Zhang, J. Wu, Y. Zhu, D.O. Dumcenco, J. Hong, N. Mao, S. Deng, Y. Chen, Y. Yang, C. Jin, S.H. Chaki, Y-S. Huang, J. Zhang, and L. Xie: Two-dimensional molybdenum tungsten diselenide alloys: Photoluminescence, Raman scattering, and electrical transport. *ACS Nano* **8**, 7130 (2014).
25. X. Wang, Y. Gong, G. Shi, W.L. Chow, K. Keyshar, G. Ye, R. Vajtai, J. Lou, Z. Liu, E. Ringe, B.K. Tay, and P.M. Ajayan: Chemical vapor deposition growth of crystalline monolayer $MoSe_2$. *ACS Nano* **8**, 5125 (2014).
26. A.A. Puretzky, L. Liang, X. Li, K. Xiao, K. Wang, M. Mahjouri-Samani, L. Basile, J.C. Idrobo, B.G. Sumpter, V. Meunier, and D.B. Geohegan: Low-frequency Raman fingerprints of two-dimensional metal dichalcogenide layer stacking configurations. *ACS Nano* **9**, 6333 (2015).
27. A.A. Puretzky, L. Liang, X. Li, K. Xiao, B.G. Sumpter, V. Meunier, and D.B. Geohegan: Twisted $MoSe_2$ bilayers with variable stacking and interlayer coupling revealed by low-frequency Raman spectroscopy. *ACS Nano* (2016), doi: 10.1021/acsnano.5b07807.